https://www.osapublishing.org/optica/viewmedia.cfm?uri=optica-5-2-213&seq=0

Research Article Vol. 5, No. 2 / February 2018 / Optica 213

High-efficiency thermophotovoltaic energy conversion enabled by a metamaterial selective emitter

David N. Woolf,[1,*] Emil A. Kadlec,[2] Don Bethke,[2] Albert D. Grine,[2] John J. Nogan,[2] Jeffrey G. Cederberg,[3] D. Bruce Burckel,[2] Ting Shan Luk,[2] Eric A. Shaner,[2] and Joel M. Hensley[1]

[1]Physical Sciences Inc., 20 New England Business Center, Andover, Massachusetts 01810-1077, USA
[2]Sandia National Laboratories, P.O. Box 5800, Albuquerque, New Mexico 87185, USA
[3]Lincoln Laboratory, Massachusetts Institute of Technology, 244 Wood Street, Lexington, Massachusetts 02421-6426, USA
*Corresponding author: dwoolf@psicorp.com

Received 4 August 2017; revised 17 November 2017; accepted 22 November 2017 (Doc. ID 304056); published 16 February 2018

Thermophotovoltaics (TPV) is the process by which photons radiated from a thermal emitter are converted into electrical power via a photovoltaic cell. Selective thermal emitters that can survive at temperatures at or above ~1000°C have the potential to greatly improve the efficiency of TPV energy conversion by restricting the emission of photons with energies below the photovoltaic (PV) cell bandgap energy. In this work, we demonstrated TPV energy conversion using a high-temperature selective emitter, dielectric filter, and 0.6 eV $In_{0.68}Ga_{0.32}As$ photovoltaic cell. We fabricated a passivated platinum and alumina frequency-selective surface by conventional stepper lithography. To our knowledge, this is the first demonstration of TPV energy conversion using a metamaterial emitter. The emitter was heated to >1000°C, and converted electrical power was measured. After accounting for geometry, we demonstrated a thermal-to-electrical power conversion efficiency of 24.1 ± 0.9% at 1055°C. We separately modeled our system consisting of a selective emitter, dielectric filter, and PV cell and found agreement with our measured efficiency and power to within 1%. Our results indicate that high-efficiency TPV generators are possible and are candidates for remote power generation, combined heat and power, and heat-scavenging applications. © 2018 Optical Society of America

OCIS codes: (160.3918) Metamaterials; (040.5350) Photovoltaic; (290.6815) Thermal emission.

https://doi.org/10.1364/OPTICA.5.000213

1. INTRODUCTION

Thermophotovoltaic (TPV) energy conversion has long been recognized for its potential to efficiently convert high-grade radiated heat (>1000°C) directly into electrical power using a photovoltaic (PV) cell. Thermophotovoltaics was initially conceived of in the 1960s ([1,2]) as a higher-temperature, higher-efficiency replacement for thermionics and thermoelectrics. TPV systems are extremely versatile; a hot emitting surface and a low-bandgap PV cell can be combined with any kind of heat source (concentrated solar energy, a radioisotope thermal generator, a combustible fuel, etc.) to generate electrical power for a wide range of applications including remote generators [3], combined heat and power systems [4,5] for homes, spacecraft power sources [6], and solar thermophotovoltaic (STPV) power for both space and terrestrial applications [7–9].

The field of thermophotovoltaics has undergone numerous evolutions, first as low-bandgap PV began improving in the mid-1980s [10] and then in the last decade with the advent of high-temperature, spectrally selective emitters [11–20]. It has generally been considered that 20% efficiency is necessary for large-scale adaptation of TPV [21], but despite its potential, only one full commercial TPV system has ever been developed [22]. Part of the reason is that TPV systems must operate in a narrow slice of parameter space. The thermal emitter must be hot enough (>800°C) such that a significant amount of the emitted power exists above the bandgap of a photovoltaic cell. However, the internal quantum efficiency of PV cells become significantly worse as their bandgap energies decrease below 0.6 eV. Even at the most favorable extremes of these limits, Wien's displacement law tells us that the peak of a 1000°C blackbody is 2.27 μm, below the 2.06 μm bandgap wavelength of a 0.6 eV PV cell, and only 20% of photons are emitted above the bandgap. As temperatures are pushed higher, the blackbody spectrum becomes better aligned with PV cells, but only certain materials with desirable optical properties have high enough melting points to survive, and even then, their optical properties when hot deviate from those at room temperature [23]. Thus, a high-efficiency TPV system must contain high-quality low-bandgap PV material, a hot-but-not-too-hot emitter, and an ability to reduce or recycle energy that is emitted below the PV bandgap.

While the thermodynamic limit of thermal-to-electrical conversion efficiency of TPV systems is greater than 50%, [9,24–26],

studies that have employed realistic spectral filtering arrived at maximum practically attainable efficiencies closer to 25% [23,27]. Recently, numerous experimental studies have been performed on high-temperature selective emitters that can help reach the 20% efficiency target. Various methods, including epsilon-near-zero metamaterials [14], photonic crystal microcavities [28,29], inverse opals [30], and frequency-selective surfaces (FSSs) [13], have been employed to restrict the radiated power from the emitter below the bandgap of the PV cell. For the highest conversion efficiencies, selective emitters are necessary but not typically sufficient, due to small but non-negligible emissivity below the photovoltaic bandgap. To further improve the conversion efficiency, selective emitters have been paired with additional spectral filtering, such as dielectric filters, to promote photon recycling [23], and the prospect of near-field energy transfer has also been explored [31–35].

In spite of this rich body of work on emitters and TPV models, very few experimental demonstrations of actual TPV power generation have been reported in this century [36–40], and many practical considerations, such as the performance of the selective emitter at high temperature, have been under-studied. In this paper, we report on an experimental demonstration of TPV energy conversion above the 20% efficiency threshold. Our experimental system consists of a passivated platinum and alumina metamaterial selective emitter (SE) by conventional stepper lithography, paired with a stand-alone dielectric filter (DF) and an $In_{0.68}Ga_{0.32}As$ five-junction monolithically integrated module (MIM) photovoltaic cell. The emitter, cemented to a cartridge heater, was heated to 1055°C, and converted electrical power was measured. By removing the effects of the geometrical view factor, we demonstrated a thermal-to-electrical power conversion efficiency of 24.1 ± 0.9% at 1055°C. This is, to our knowledge, the first demonstration of TPV energy conversion utilizing a metamaterial emitter. We separately modeled our system consisting of a SE, DF, and PV cell and found agreement with our measured efficiency and power to within our margin of error.

Our chosen SE consists of an array of platinum pucks (diameter $d = 250$ nm, pitch $p = 650$ nm, height $h = 45$ nm) separated from a platinum backplane ($t_b = 200$ nm) by a layer of alumina ($s = 90$ nm) and encapsulated by an additional conformal layer of alumina ($t_e = 150$ nm). The initial platinum and alumina layers were deposited on a 100 mm diameter, 0.65 mm thick C-plane single-side polished sapphire wafer (MTI ALC100D065C1) using electron-beam evaporation. The wafer was rinsed with solvents and cleaned in O_2 plasma for 15 min prior to deposition. A 3 nm thick chrome sticking layer was deposited under the platinum backplane to promote adhesion to the substrate. After deposition, an antireflection coating (ARC) and positive photoresist were spin-coated onto the substrate. The substrate was patterned using deep-UV stepper lithography, followed by development of the photoresist and stripping of the ARC using N-methyl-2-pyrrolidone (NMP) (Microchem). In typical wafer processing, tetramethylammonium hydroxide (TMAH) would be used instead of NMP, as NMP can leave behind resist residue. However, we found that TMAH etches alumina as well. To remove the resist residue, a 40 s O_2 plasma descum was performed in a reactive ion etcher (RIE). This was followed by the deposition of the top platinum layer without a chrome adhesion layer, removal of the photoresist, reveal of the pattern by liftoff, and O_2 plasma clean. We then grew a 150 nm alumina encapsulation layer by atomic layer deposition (ALD) and diced the wafer into 18 mm × 18 mm square pieces for measurement.

An optical image of a mounted SE die and an scanning electron microscope (SEM) image of a portion of it are shown in Figs. 1(a) and 1(b), respectively. Details of the emitter design have been published previously [13]. The emitter in Fig. 1(a) is mounted on a cartridge heater with integrated thermocouple (HeatWaveLabs) capable of heating to 1200°C. Two additional thermocouples [one shown in Fig. 1(a)] are epoxied to the exposed heater surface, directly next to the emitter. The mounted sample is part of a larger experimental apparatus shown in Fig. 1(c). A circular aperture of radius $r_{ap} = 5$ mm and thickness $t_{ap} = 1.75$ mm is located $h_{ap} = 6.35$ mm above the emitter to prevent emission from any other hot surface from reaching the detector. The detector was mounted on a vertical translation stage at height h above the emitter to control and calibrate the separation. All distances were measured using a digital micrometer and are accurate to better than 0.1 mm. The lateral alignment between the aperture and the detector was accurate to 1 mm.

A custom DF designed to be highly transmissive between 1 and 2 μm and reflective between 2 and 5 μm was placed on top of the aperture in experiments using the SE. The DF consists of alternating high and low index layers sandwiched between calcium fluoride (CaF_2) sub- and superstrates. The glue that holds the super and substrates together has small absorption features between 2.5 and 3.5 μm that absorb less than 1% of the total emitted power. The modeled transmission, reflection, and absorption of the filter at normal incidence are shown in Supplement 1, Fig. S1.

Two different detectors were used in the experiments. In addition to the five-junction InGaAs PV cell, a ThorLabs S302C thermal power meter (TPM) with flat responsivity ~98% throughout the infrared was used to calibrate the emission from the emitters. The cartridge heater, aperture, and detector are each

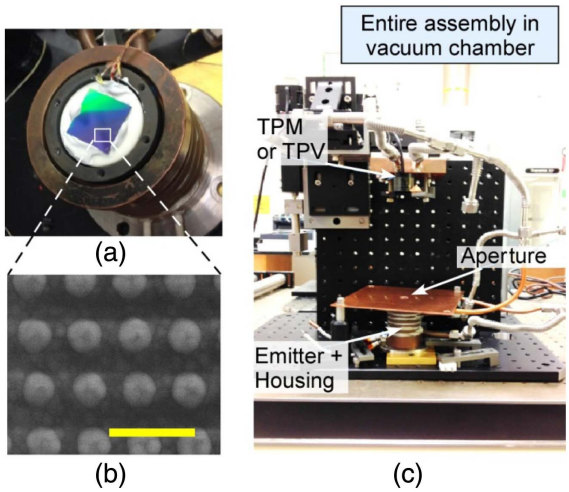

Fig. 1. (a) Image of the selective emitter (SE) mounted on a water-chilled cartridge heater. SE die is 18 mm × 18 mm. (b) SEM of metamaterial SE. Scale bar is 1 μm. (c) Experimental apparatus showing the emitter and heater housing mounted on a breadboard beneath a copper plate with a 10 mm diameter aperture cut out. A detector (either a TPM or a PV cell) is mounted to a vertically oriented breadboard by a linear translation stage. The entire setup is housed inside a vacuum chamber.

cooled by house-chilled water at 9°C. The entire apparatus is housed in a vacuum chamber whose pressure is maintained at 1e-3 torr throughout the experiments.

The temperature of each of the three heater thermocouples, the power delivered to the heater, the output of the power meter, and the temperature of the power meter were recorded as a function of time. The power supplied to the heater was gradually increased over approximately 1 h until the temperature of the emitter surface exceeded 1000°C. The two thermocouples measuring the temperature of the emitter surface agreed to within 1% throughout the operating range and differed by an average of 0.8% (see Supplement 1, Fig. S2) above 800°C.

A Si chip with known emissivity [41,42] was used to characterize our geometric view factor (VF): the fraction of power radiated from the hot emitter that is collected by the detector.

The view factor for a Lambertian emitter is calculated as

$$\mathrm{VF} = \frac{1}{A_{\mathrm{emit}}} \int_{A_{\mathrm{emit}}} \mathrm{d}A_{\mathrm{emit}} \int_{A_{\mathrm{det}}} \mathrm{d}F, \tag{1}$$

where A_{emit} and A_{det} are the areas of the emitter and detector, respectively, and dF is the fraction of radiation from area dA_{emit} incident on area dA_{det}. For a Lambertian emitter,

$$dF = \frac{\cos^2(\theta)}{2\pi l^2 \int_0^{\pi/2} \sin(\theta)\cos(\theta)\mathrm{d}\theta} \mathrm{d}A_{\mathrm{det}}, \tag{2}$$

where θ is the angle between the surface normal and the ray of length $l = h/\cos(\theta)$ connecting dA_{det} and dA_{emit}. We use an additional restriction in our calculation of VF, removing all rays that do not pass through the aperture. The geometry for the VF calculation is shown in Fig. 2(a). The view factor is necessary to calculate because it relates the power collected in a tabletop geometry, such as this experiment where VF $\ll 1$ to one in a complete system where VF ~ 1.

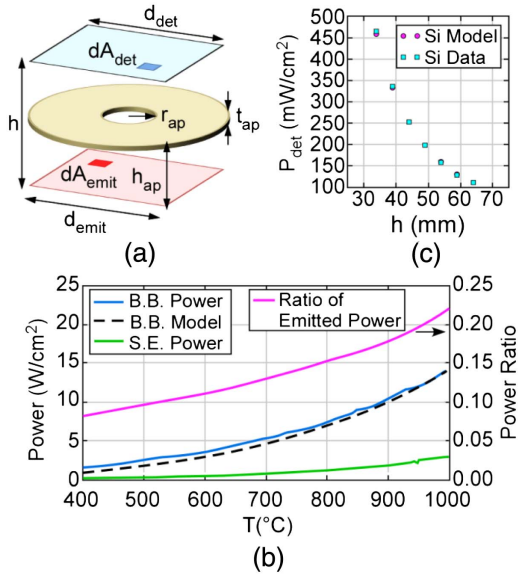

Fig. 2. (a) Geometry for view factor (VF) calculation, where h is the separation between the emitter and detector, h_{ap} is the height of the aperture above the emitter, t_{ap} is the thickness of the aperture, and d_{emit} and d_{det} are the diameters of the emitter and detector, respectively. (b) Power emitted by a blackbody (blue solid line) and the SE (green solid line), determined by dividing the measured power by VF, are plotted along the left vertical axis along with the blackbody power (dashed black line) as determined by the Stefan–Boltzmann Law. The ratio of the SE to the blackbody power is plotted along the right vertical axis (magenta line). (c) Power received by the selective emitter (circles) and power expected (squares) based on measured geometry and temperature for various values of h.

Figure 2(b) compares the optical power emitted by our SE to the optical power emitted by a blackbody. The solid blue curve is the radiosity of the blackbody, calculated as $P_{bb} = P_{\mathrm{rec}}/\varepsilon \mathrm{VF}_{\mathrm{Si}}$, where P_{rec} is the power received by the TPM from the Si emitter, ε is the emissivity of silicon, and $\mathrm{VF}_{\mathrm{Si}} = 6.3 \times 10^{-3}$ is the view factor of the Si-detector system when $h = 42.9$ mm. The expected radiosity of a blackbody (dashed black line) is calculated from the Stefan–Boltzmann relation, $P = \sigma T^4$; σ is the Stefan–Boltzmann constant, and T is the temperature in Kelvin. We also compared the model and measurement as a function of emitter–detector separation [Fig. 2(c)]. Because VF has a complex functional form, comparisons between this data and theory give a highly sensitive (see Supplement 1, Fig. S3) method of confirming proper calibration of the measurement geometry. The measured separation matches the separation corresponding to best agreement between the data points in Fig. 2(c) to 0.1 mm, and P_{bb} differed from P_{rec} by an average 3.6%. This translates directly to the ±0.9% margin of error in our efficiency measurements. No fitting parameters on either the geometry or the temperature were used to force agreement between expected and measured power.

With the geometry well calibrated, we can compare our SE with unknown emissivity to a known Si emitter using direct measurements of geometry, without fitting, to calculate the view factor. The green curve in Fig. 2(b) represents the radiosity of the SE–DF system and is calculated by $P_{\text{SE-DF}} = P_{\mathrm{det}}/\mathrm{VF}_{\text{SE-DF}}$, where P_{det} is the power received by the TPM and $\mathrm{VF}_{\text{SE-DF}} = 2.2 \times 10^{-3}$ is the view factor of the SE–DF–detector system when $h = 67.9$ mm. The power ratio (PR), representing the restriction of power transmission by the spectrally SE–DF system when compared to a blackbody is given by

$$\mathrm{PR}(T) = \frac{P_{\text{SE-DF}}(T)}{P_{bb}(T)} \tag{3}$$

and is plotted along the right vertical axis (magenta curve) as a function of temperature. The SE–DF tandem transmits a larger fraction of the blackbody's power as the emitter temperature increases and the SE–DF transmission function overlaps more with the blackbody power spectrum, reaching 21% of the power of the blackbody at 1000°C. In experiments without the DF, the selective emitter emitted 53% less power than a blackbody.

Next, we replaced the TPM with the photovoltaic cell. Our mounted, 0.6 eV bandgap 3.5 × 4.2 mm InGaAs PV cell is pictured in Fig. 3(a). The PV cell was positioned 16 mm above the top of the aperture. The temperature of the emitter surface was gradually increased to 1055°C over approximately 1 h. During the ramp-up, the temperature was allowed to equilibrate periodically and current–voltage (IV) curves were collected [Fig. 3(b)]. The IV curves reveal a cell with open circuit voltage $V_{\mathrm{OC}} = 0.377$ V/junction and fill factor FF = 0.699 for short circuit current $I_{\mathrm{SC}} = 21.1$ mA at 1055°C. The geometric view factor for the SE–DF–PV system was calculated to be 0.066 when $h = 16$ mm using Eqs. (1) and (2) as before. The 0.1 mm difference between the measured emitter–PV separation and the best-agreement emitter–PV separation corresponds to a 1.3% change in VF. The difference between the measured temperature and the best-agreement temperature was 1°C. These errors combined

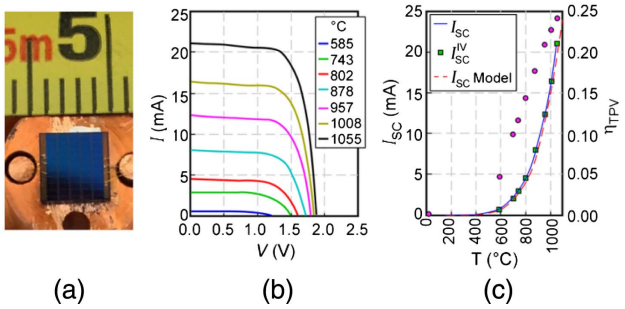

Fig. 3. (a) Image of PV cell. (b) IV curves taken for emitters at various temperatures. (c) Short circuit current (I_{SC}) as continuously sampled (blue line) during the gradual increase of SE temperature, as taken from the IV curves shown in (b) (green squares), and as calculated based on our model (red dashed line), plotted against the left vertical axis. Thermal-to-electric conversion efficiency η_{TPV} (circles) is plotted along the right vertical axis.

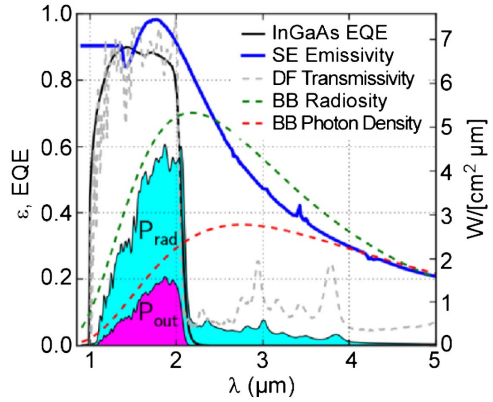

Fig. 4. Spectral properties of the components of our TPV system. The emissivity of the SE (blue), transmissivity of the DF (gray dashed) and EQE of the PV cell (black) are all plotted along the left vertical axis. The blackbody spectral radiosity (green dashed) and photon flux (red dashed), normalized to $qV_{OC}FF$, are plotted along the right vertical axis for a surface at 1055°C. The forward power transmitted by the SE–DF system is represented by the cyan shaded area. The power generated by the PV cell is represented by the magenta shaded area, and η_{TPV} is represented by the ratio of the two areas.

result in an absolute uncertainty in our subsequent efficiency calculation of ±0.2%.

At 1055°C, the power collected P_{out} was 39.8 mW (0.27 W/cm^2). Note that this is roughly 25% of the power expected from a blackbody radiator at this temperature with VF = 1. Thus, because $A_{cell} \ll A_{emit}$, the PV cell is operating near the thermal and photonic load of a field implementation despite the 16 mm gap between our SE and the PV cell.

With these measurements, we can now estimate the efficiency of a complete system with VF = 1. This is equivalent to defining the efficiency as the ratio of electrical power generated by the PV cell (P_{out}) to the amount of power incident on the cell (P_{in}). The amount of power radiated per unit area by our selective emitter is $PR(T)P_{bb}(T)$. The thermophotovoltaic efficiency is defined as

$$\eta_{TPV}(T) = \frac{P_{out}(T)}{P_{in}(T)} = \frac{P_{out}(T)/A_{PV}}{PR(T)P_{bb}(T)} \quad (4)$$

and is plotted in Fig. 3(c). P_{out} was calculated by finding $[IV]_{max}$ from the current–voltage sweeps. According to our measurements, a TPV device with VF = 1 should have a thermal-to-electric conversion efficiency of 22.5% at 1008°C and 24.1% at 1055°C.

These results are internally consistent with a system model that we built based on earlier emissivity measurements (Fig. 4). In this figure, plotted along the left vertical axis, the black curve represents the external quantum efficiency (EQE) of the PV cell, the gray dashed curve is the transmissivity of the DF, and the blue curve is the emissivity of the SE. The SE emissivity was measured using an imaging Fourier Transform InfraRed (FTIR) spectrometer. Here a silicon reference emitter with known emissivity in thermal equilibrium with the selective emitter was used to calibrate the detector. The reference emitter and the selective emitter were mounted on a rotation stage such that either emitter could be placed in the optical path of the FTIR without adjusting any optics (see Supplement 1, Fig. S4). The combination of the beam splitter and detector in the FTIR led to a weak signal at short wavelengths, and correspondingly, a high level of uncertainty in the absolute value of the peak of the emission, although from room temperature reflectivity measurements we determine this value to be ~0.95. No data was obtained below 1.3 μm, so the curve was extended at a fixed value of 0.9 to shorter wavelengths.

The green and red dashed lines in Fig. 4 are the blackbody radiosity, P_{rad}, and blackbody photon flux density (normalized by $qV_{OC}FF$ to put in units of W/cm^2 μm) at 1050°C, respectively. The cyan shaded area represents the total power transmitted by the SE–DF system, while photon flux density normalization allows the shaded magenta area to the electrical power out on the same axis as P_{rad}. Each of these curves are plotted along the right vertical axis. Shown this way, the thermal-to-electrical conversion efficiency is simply the ratio of the areas of the cyan and magenta shaded regions.

Because VF ≪ 1 in the experimental configuration, we ignore the effects of multiple reflections from the mirrored back surface of the PV, the DF, and reemission from the SE.

Our model predicts a photovoltaic conversion efficiency is 23.3% for an emitter at 1055°C, within 0.8% of the efficiency measured without the model. Without the DF, the efficiency drops to 15.4%. With the DF alone (no SE), the efficiency is only 12.1%. With our model, we can also estimate the spectral efficiency of the total system, defined as the fraction of photons received by the PV cell that are above the bandgap: $\eta_{spec} = n_{absorbed}/n_{emitted}$. We find that 70% of emitted photons are absorbed by the PV cell above the bandgap.

A prototype TPV converter will differ in a few key ways from our experiment. First, the thermal and photonic load experienced by the PV cell will be larger due to the increased VF. Based on data collected on similar PV cells [43,44] and extrapolation from our data to unity VF, we expect V_{OC} to approach 0.4 V/junction under full illumination at 1055°C, equivalent to increasing the thermal-to-electric conversion efficiency from 24.1 to 25.7%. This increase in efficiency will help offset the higher PV operating temperature associated with the increased photonic load and heat conducted via the walls of the TPV converter from the emitter to the PV cells, and other balance of plant considerations, such as

losses due to series and shunt resistances, that work to reduce the overall system efficiency in a functioning device.

Second, multiple reflections from the optical cavity consisting of emitter, filter, and PV cell with metal back-reflector can have a strong effect on the transfer function, especially if there is competition between cavities, such as between an emitter and the DF and between the DF and a back-reflector on the PV cell. The transmissivity function S of a multi-cavity system is written as

$$S \approx \sum_{i=0}^{\infty}\sum_{j=0}^{\infty}\sum_{k=0}^{\infty} \epsilon T_F [R_F(1-\epsilon)]^i [R_F R_{\mathrm{PV}}]^j [T_F^2 R_{\mathrm{PV}}(1-\epsilon)]^k, \quad (5)$$

where ϵ is the emissivity of the emitter; T_F and R_F are the transmissivity and reflectivity of the DF and $T_F = 1–R_F$, respectively, assuming no absorption in the DF; and $R_{\mathrm{PV}} = 1 - \mathrm{EQE}$ above bandgap and R_{BF} below bandgap. For a high-R_{BF} PV cell, most of the selective emitter's below-bandgap radiation ultimately reaches the PV cell due to the high quality factor of the cavity formed by the DF and SE, rendering the DF useless. However, a system with a poorly reflecting back reflector will result in only a modest drop in efficiency (~2% absolute). Improvements to the performance of the DF and SE below bandgap or choosing a different cavity configuration would reduce this reduction of the conversion efficiency.

Third, while our experiments were performed in a vacuum chamber, a final device configuration will likely preclude vacuum operation due to associated costs. Operation in a noble gas ambient with an emitter–detector standoff of a few cm is a sufficient alternative, allowing radiative heat transfer between the emitter and PV to dominate over conductive heat transfer.

Fourth, the ultimate efficiency of fuel-based TPV power generators also depends on the efficient conversion of chemical fuel energy into usable thermal energy. Combustors using a catalyst and recuperator to reclaim the energy otherwise lost in hot exhaust gasses have been shown to have chemical-to-thermal conversion efficiencies greater than 80% [45,46], making 20%-efficient TPV generators attainable with our emitter-filter combination.

Ultimately, TPV devices will need to be efficient and have long lifetimes to rise beyond niche applications. Throughout these experiments, the SE underwent more than two dozen thermal cycles and spent more than 2 h over 1000°C. Separate tests after six thermal cycles and 2 total hours in an argon atmosphere at 1000°C showed that physical morphology changes were limited to a slight increase in surface roughness to a root mean squared value of 5 A as determined by atomic force microscopy and only after the first exposure to temperature. SEM images revealed discoloration of the encapsulation layer, indicating some reflowing and stress in the emitter, but no change in the pattern. Optical images also indicated this, showing an initial color change followed by an increase in visible haze after thermal cycling, likely due to the increase in roughness, but no additional change in color, which previous results indicate correlate very strongly with underlying morphology changes [13] (see Supplement 1, Fig. S5).

In conclusion, we have demonstrated TPV power generation using a selective emitter at 1055°C (1328 K), dielectric filter, and 0.6 eV $In_{0.68}Ga_{0.32}As$ photovoltaic cell, generating 0.189 W/cm^2. The selective emitter was fabricated out of Pt and Al_2O_3 layers using conventional photolithographic techniques that will allow us to affordably scale the fabrication. Using a geometric view function, we determined that 24.1% of the radiation incident on the PV cell was converted into electricity. We closely matched our experimental performance to a model of the TPV system, which indicated that 70% of the photons transmitted by the SE–DF system were absorbed by the PV cell. The model was also used to understand how our experiment would extrapolate to a completed device. Our results are a promising step toward realizing a high-performance TPV converter.

Funding. Office of Naval Research (ONR) (N00014-15-C-0041); National Nuclear Security Administration (NNSA) (DE-NA0003525); Center for Integrated Nanotechnologies (CINT).

Acknowledgment. Any opinions, findings, conclusions, or recommendations expressed in this material are those of the authors and do not necessarily reflect the views of the ONR. This work was performed, in part, at the CINT, an Office of Science User Facility operated for the U.S. Department of Energy (DOE) Office of Science. Sandia National Laboratories is a multimission laboratory managed and operated by National Technology and Engineering Solutions of Sandia LLC, a wholly owned subsidiary of Honeywell International Inc. for the U.S. Department of Energy's National Nuclear Security Administration.

See Supplement 1 for supporting content.

REFERENCES

1. P. Aigrain, "The thermophotovoltaic converter," (1960) (unpublished lectures given at MIT).
2. B. D. Wedlock, "Thermo-photo-voltaic energy conversion," Proc. IEEE **51**, 694–698 (1963).
3. W. Chan, R. Huang, C. Wang, J. Kassakian, J. Joannopoulos, and I. Celanovic, "Modeling low-bandgap thermophotovoltaic diodes for high-efficiency portable power generators," Solar Energy Mater. Solar Cells **94**, 509–514 (2010).
4. L. M. Fraas, J. E. Avery, and H. X. Huang, "Thermophotovoltaic furnace-generator for the home using low bandgap GaSb cells," Semicond. Sci. Technol. **18**, S247–S253 (2003).
5. M. Bianchi, C. Ferrari, F. Melino, and A. Peretto, "Feasibility study of a thermo-photo-voltaic system for CHP application in residential buildings," Appl. Energy **97**, 704–713 (2012).
6. C. J. Crowley, N. A. Elkouh, S. Murray, D. L. Chubb, M. S. El-Genk, and M. J. Bragg, "Thermophotovoltaic converter performance for radioisotope power systems," AIP Conf. Proc. **746**, 601–614 (2005).
7. A. Lenert, Y. Nam, D. M. Bierman, and E. N. Wang, "Role of spectral non-idealities in the design of solar thermophotovoltaics," Opt. Express **22**, A1604–A1618 (2014).
8. C. Wu, B. Neuner III, J. John, A. Milder, B. Zollars, S. Savoy, and G. Shvets, "Metamaterial-based integrated plasmonic absorber/emitter for solar thermo-photovoltaic systems," J. Opt. **14**, 024005 (2012).
9. E. Rephaeli and S. Fan, "Absorber and emitter for solar thermo-photovoltaic systems to achieve efficiency exceeding the Shockley-Queisser limit," Opt. Express **17**, 15145–15159 (2009).
10. L. D. Woolf, "Optimum efficiency of single and multiple bandgap cells in thermophotovoltaic energy conversion," Sol. Cells **19**, 19–38 (1986).
11. C. Shemelya, D. DeMeo, N. P. Latham, X. Wu, C. Bingham, W. Padilla, and T. E. Vandervelde, "Stable high temperature metamaterial emitters for thermophotovoltaic applications," Appl. Phys. Lett. **104**, 201113 (2014).
12. X. Liu, T. Tyler, T. Starr, A. F. Starr, N. M. Jokerst, and W. J. Padilla, "Taming the blackbody with infrared metamaterials as selective thermal emitters," Phys. Rev. Lett. **107**, 045901 (2011).
13. D. Woolf, J. Hensley, J. G. Cederberg, D. T. Bethke, A. D. Grine, and E. A. Shaner, "Heterogeneous metasurface for high temperature selective emission," Appl. Phys. Lett. **105**, 081110 (2014).

14. S. Molesky, C. W. Dewalt, and Z. Jacob, "High temperature epsilon-near-zero and epsilon-near-pole metamaterial emitters for thermophotovoltaics," Opt. Express **21**, A96–A110 (2013).
15. E. S. Sakr, Z. Zhou, and P. Bermel, "High efficiency rare-earth emitter for thermophotovoltaic applications," Appl. Phys. Lett. **105**, 111107 (2014).
16. I. Celanovic, F. O'Sullivan, M. Ilak, J. Kassakian, and D. Perreault, "Design and optimization of one-dimensional photonic crystals for thermophotovoltaic applications," Opt. Lett. **29**, 863–865 (2004).
17. S. Pendharker, H. Hu, S. Molesky, R. Starko-Bowes, Z. Poursoti, S. Pramanik, N. Nazemifard, R. Fedosejevs, T. Thundat, and Z. Jacob, "Thermal graphene metamaterials and epsilon-near-zero high temperature plasmonics," J. Opt. **19**, 055101 (2017).
18. Y. Nam, Y. X. Yeng, A. Lenert, P. Bermel, I. Celanovic, M. Soljačić, and E. N. Wang, "Solar thermophotovoltaic energy conversion systems with two-dimensional tantalum photonic crystal absorbers and emitters," Solar Energy Mater. Solar Cells **122**, 287–296 (2014).
19. Y. B. Chen and Z. M. Zhang, "Design of tungsten complex gratings for thermophotovoltaic radiators," Opt. Commun. **269**, 411–417 (2007).
20. V. Rinnerbauer, Y. X. Yeng, W. R. Chan, J. J. Senkevich, J. D. Joannopoulos, M. Soljačić, and I. Celanovic, "High-temperature stability and selective thermal emission of polycrystalline tantalum photonic crystals," Opt. Express **21**, 11482–11491 (2013).
21. T. J. Coutts and J. S. Ward, "Thermophotovoltaic and photovoltaic conversion at high-flux densities," IEEE Trans. Electron Devices **46**, 2145–2153 (1999).
22. L. M. Fraas, J. E. Avery, and H. X. Huang, "Thermophotovoltaics: Heat and electric power from low bandgap "solar" cells around gas fired radiant tube burners," in *Conference Record of the 29th IEEE Photovoltaic Specialists Conference* (2002), pp. 1553–1556.
23. Y. X. Yeng, W. R. Chan, V. Rinnerbauer, J. D. Joannopoulos, M. Soljačić, and I. Celanovic, "Performance analysis of experimentally viable photonic crystal enhanced thermophotovoltaic systems," Opt. Express **21**, A1035–A1051 (2013).
24. E. Nefzaoui, J. Drevillon, and K. Joulain, "Selective emitters design and optimization for thermophotovoltaic applications," J. Appl. Phys. **111**, 084316 (2012).
25. V. Ganapati, T. P. Xiao, and E. Yablonovitch, "Ultra-efficient thermophotovoltaics exploiting spectral filtering by the photovoltaic band-edge," arXiv: 1611.03544 (2016).
26. A. Polman and H. A. Atwater, "Photonic design principles for ultrahigh-efficiency photovoltaics," Nat. Mater. **11**, 174–177 (2012).
27. P. Bermel, M. Ghebrebrhan, W. Chan, Y. X. Yeng, M. Araghchini, R. Hamam, C. H. Marton, K. F. Jensen, M. Soljačić, and J. D. Joannopoulos, "Design and global optimization of high-efficiency thermophotovoltaic systems," Opt. Express **18**, A314–A334 (2010).
28. H. Sai and H. Yugami, "Thermophotovoltaic generation with selective radiators based on tungsten surface gratings," Appl. Phys. Lett. **85**, 3399–3401 (2004).
29. S. Y. Lin, J. Moreno, and J. G. Fleming, "Three-dimensional photonic-crystal emitter for thermal photovoltaic power generation," Appl. Phys. Lett. **83**, 380–382 (2003).
30. K. A. Arpin, M. D. Losego, A. N. Cloud, H. Ning, J. Mallek, N. P. Sergeant, L. Zhu, Z. Yu, B. Kalanyan, and G. N. Parsons, "Three-dimensional self-assembled photonic crystals with high temperature stability for thermal emission modification," Nat. Commun. **4**, 2630 (2013).
31. S. Basu, Y. B. Chen, and Z. M. Zhang, "Microscale radiation in thermophotovoltaic devices—a review," Int. J. Energy Res. **31**, 689–716 (2007).
32. M. Laroche, R. Carminati, and J. J. Greffet, "Near-field thermophotovoltaic energy conversion," J. Appl. Phys. **100**, 063704 (2006).
33. A. W. Rodriguez, O. Ilic, P. Bermel, I. Celanovic, J. D. Joannopoulos, M. Soljačić, and S. G. Johnson, "Frequency-selective near-field radiative heat transfer between photonic crystal slabs: a computational approach for arbitrary geometries and materials," Phys. Rev. Lett. **107**, 114302 (2011).
34. O. Ilic, M. Jablan, J. D. Joannopoulos, I. Celanovic, and M. Soljačić, "Overcoming the black body limit in plasmonic and graphene near-field thermophotovoltaic systems," Opt. Express **20**, A366–A384 (2012).
35. T. J. Bright, L. P. Wang, and Z. M. Zhang, "Performance of near-field thermophotovoltaic cells enhanced with a backside reflector," J. Heat Transfer **136**, 062701 (2014).
36. L. M. Fraas, J. E. Samaras, X. H. Huang, L. M. Minkin, J. E. Avery, W. E. Daniels, and S. Hui, "TPV generators using the radiant tube burner configuration," in *17th European PV Solar Energy Conference*, Munich, Germany, Oct. 22–26, 2001.
37. A. Lenert, D. M. Bierman, Y. Nam, W. R. Chan, I. Celanović, M. Soljačić, and E. N. Wang, "A nanophotonic solar thermophotovoltaic device," Nat. Nanotechnol. **9**, 126–130 (2014).
38. W. R. Chan, P. Bermel, R. C. N. Pilawa-Podgurski, C. H. Marton, K. F. Jensen, J. J. Senkevich, J. D. Joannopoulos, M. Soljačić, and I. Celanovic, "Toward high-energy-density, high-efficiency, and moderate-temperature chip-scale thermophotovoltaics," Proc. Natl. Acad. Sci. USA **110**, 5309–5314 (2013).
39. B. Wernsman, R. R. Siergiej, S. D. Link, R. G. Mahorter, M. N. Palmisiano, R. J. Wehrer, R. W. Schultz, G. P. Schmuck, R. L. Messham, and S. Murray, "Greater than 20% radiant heat conversion efficiency of a thermophotovoltaic radiator/module system using reflective spectral control," IEEE Trans. Electron Devices **51**, 512–515 (2004).
40. M. W. Yang, K. J. Chua, J. F. Pan, D. Y. Jiang, and H. An, "Development of micro-thermophotovoltaic power generator with heat recuperation," Energy Convers. Manage. **78**, 81–87 (2014).
41. T. Satō, "Spectral emissivity of silicon," Jpn. J. Appl. Phys. **6**, 339–347 (1967).
42. N. M. Ravindra, S. Abedrabbo, W. Chen, F. M. Tong, A. K. Nanda, and A. C. Speranza, "Temperature-dependent emissivity of silicon-related materials and structures," IEEE Trans. Semicond. Manuf. **11**, 30–39 (1998).
43. J. G. Cederberg, J. D. Blaich, G. R. Girard, S. R. Lee, D. P. Nelson, and C. S. Murray, "The development of (InGa) As thermophotovoltaic cells on InP using strain-relaxed In (PAs) buffers," J. Cryst. Growth **310**, 3453–3458 (2008).
44. J. G. Cederberg, G. R. Girard, S. R. Lee, J. E. Strauch, and G. A. Ten Eyck, "Inverted monolithic interconnected module (MIM) thermo-photovoltaics (TPV) for remote power generation," Report No. SAND2008-6462 (SAND, 2008).
45. Y. Ju and K. Maruta, "Microscale combustion: technology development and fundamental research," Prog. Energy Combust. Sci. **37**, 669–715 (2011).
46. H. Daneshvar, R. Prinja, and N. P. Kherani, "Thermophotovoltaics: fundamentals, challenges and prospects," Appl. Energy **159**, 560–575 (2015).

66.171.37.91 {ts '2018-03-25 08:59:20'}